

## Asymmetric Sodiophilic Host Based on a Ag-Modified Carbon Fiber Framework for Dendrite-Free Sodium Metal Anodes

Lulu Mo, Ai-Long Chen, Yue Ouyang, Wei Zong, Yue-E Miao,\* and Tianxi Liu\*

Cite This: *ACS Appl. Mater. Interfaces* 2021, 13, 48634–48642

Read Online

ACCESS |



Metrics &amp; More



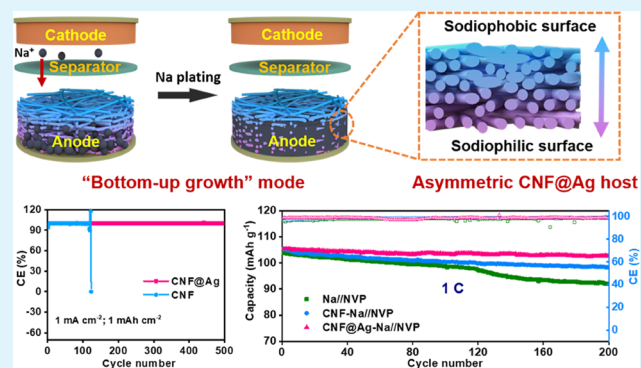
Article Recommendations



Supporting Information

**ABSTRACT:** Sodium (Na) metal is considered a promising anode material for high-energy Na batteries due to its high theoretical capacity and abundant resources. However, uncontrollable dendrite growth during the repeated Na plating/stripping process leads to the issues of low Coulombic efficiency and short circuits, impeding the practical applications of Na metal anodes. Herein, we propose a silver-modified carbon nanofiber (CNF@Ag) host with asymmetric sodiophilic features to effectively improve the deposition behavior of Na metal. Both density functional theory (DFT) calculations and experiment results demonstrate that Na metal can preferentially nucleate on the sodiophilic surface with Ag nanoparticles and uniformly deposit on the whole CNF@Ag host with a “bottom-up growth” mode, thus preventing unsafe dendrite growth at the anode/separator interface. The optimized CNF@Ag framework exhibits an excellent average Coulombic efficiency of 99.9% for 500 cycles during Na plating/stripping at  $1 \text{ mA cm}^{-2}$  for  $1 \text{ mAh cm}^{-2}$ . Moreover, the CNF@Ag-Na symmetric cell displays stable cycling for 500 h with a low voltage hysteresis at  $2 \text{ mA cm}^{-2}$ . The CNF@Ag-Na/ $\text{Na}_3\text{V}_2(\text{PO}_4)_3$  full cell also presents a high reversible specific capacity of  $102.7 \text{ mAh g}^{-1}$  for over 200 cycles at 1 C. Therefore, asymmetric sodiophilic engineering presents a facile and efficient approach for developing high-performance Na batteries with high safety and stable cycling performance.

**KEYWORDS:** carbon nanofibers, electrospinning, asymmetric structure, sodiophilic silver, sodium metal anode



## 1. INTRODUCTION

Lithium-ion batteries (LIBs) have been widely applied in portable electronic products and electric vehicles due to their high energy density and long cycle life.<sup>1,2</sup> However, the limited reserve and increasing cost of lithium resources make LIBs hard to meet fast-growing consumer markets and large-scale energy storage applications.<sup>3</sup> For this reason, sodium-ion batteries (SIBs) are regarded as promising alternatives to LIBs because of their similar electrochemical storage mechanism, low cost, and natural abundance of sodium (Na) resources.<sup>4,5</sup> For the choices of anode materials, Na metal with a high theoretical specific capacity of  $1166 \text{ mAh g}^{-1}$  and a low redox potential of  $-2.71 \text{ V}$  (vs standard hydrogen electrode) is considered the most ideal anode for constructing high-energy and low-cost SIBs.<sup>6,7</sup> In addition, the Na metal anode is a key component for other advanced Na-based batteries, such as Na-S, Na-O<sub>2</sub>, and Na-CO<sub>2</sub> batteries.<sup>8</sup> Therefore, the development of Na metal anodes is attracting considerable attention.

Unfortunately, the Na metal anode still faces severe problems in its practical applications.<sup>9,10</sup> During the cycling process, uneven Na plating/stripping, unstable solid electrolyte interphase (SEI), and large volume expansion can induce Na dendrite growth and active Na loss, eventually leading to low

Coulombic efficiency (CE), short cycling life, and safety hazards.<sup>11,12</sup> To address the abovementioned issues, various strategies have been employed, mainly including the optimization of liquid electrolytes,<sup>13,14</sup> the introduction of artificial SEI films on the Na metal surface,<sup>15,16</sup> the use of solid-state electrolytes,<sup>17</sup> and the construction of three-dimensional (3D) conductive hosts.<sup>18–21</sup> Among them, three-dimensional (3D) hosts have the merits of good conductivity and large surface area, which can not only significantly reduce the local current density but also alleviate the Na volume change during cycling. Thus, Na dendrite growth can be effectively suppressed and the CE of the Na metal anode can be largely improved.<sup>22</sup> However, the ongoing obstacle is that Na metal prefers to deposit on the top surface of most 3D hosts due to the stronger electric field and shorter Na<sup>+</sup> diffusion length in the anode area near the separators, similar to the reported “top growth” mode of Li metal plating.<sup>23,24</sup> Since the ionic radius

Received: July 9, 2021

Accepted: September 28, 2021

Published: October 11, 2021



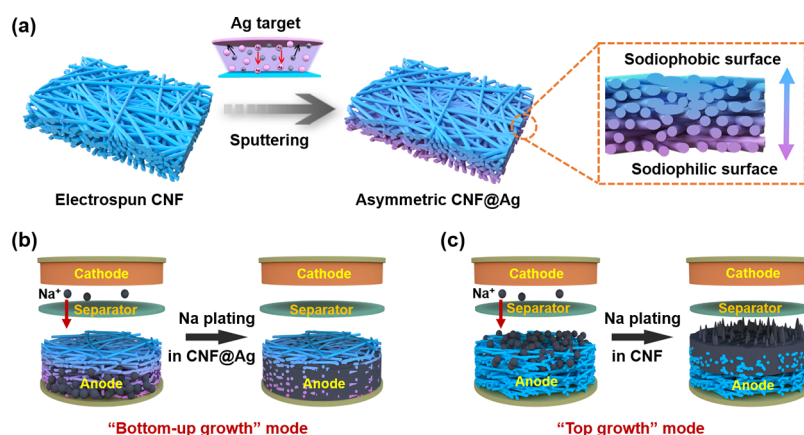


**Figure 1.** (a) Schematic showing the preparation process of the asymmetric CNF@Ag host. Na plating behavior illustrations on different hosts for Na metal batteries: (b) CNF@Ag and (c) CNF.

(1.02 Å) of  $\text{Na}^+$  is relatively large compared with that (0.76 Å) of  $\text{Li}^+$ ,  $\text{Na}^+$  mobility is lower. Based on Sand's time model,<sup>10,12</sup> slower  $\text{Na}^+$  mobility would cause the higher concentration gradient along the thickness direction of the anode, thus leading to a more severe "top growth" issue during the Na plating process. The "top growth" issue of Na deposition could accelerate dendrite penetration through the separator and increase short circuit risks.<sup>25,26</sup> Therefore, it is of great significance to reasonably regulate Na deposition far away from the unsafe anode/separator interface by optimizing the Na host structure.

Herein, a 3D host with asymmetric sodiophilic features is designed to regulate the deposition behavior of Na metal, as illustrated in Figure 1a. The asymmetric host involves an electrospun carbon nanofiber (CNF) host by sputtering Ag nanoparticles only on its separator-away surface, which is denoted CNF@Ag. With high porosity and good conductivity, the as-designed CNF@Ag host is expected to alleviate the large volume expansion of Na and regulate the local current density during the plating process, thus improving the cycling stability of the Na metal anode. Moreover, density functional theory (DFT) calculations demonstrate that the sputtered Ag nanoparticles possess higher sodiophilicity and a lower nucleation barrier than the bare CNF. Such a sodiophilic surface is preferred for Na metal nucleation and deposition on the CNF@Ag host with a desirable "bottom-up growth" mode (Figure 1b) instead of the "top growth" Na plating on the CNF host (Figure 1c). Therefore, the design of the asymmetric CNF@Ag host is an effective strategy to avoid unsafe anode/separator interface dendrite growth, indicating great potential in improving the safety and lifetime of the Na metal anode.

## 2. EXPERIMENTAL SECTION

### 2.1. Preparation of CNF and Asymmetric CNF@Ag Hosts.

The CNF membrane was prepared by a traditional electrospinning method.<sup>27–29</sup> Typically, 2 g of polyacrylonitrile (PAN,  $M_w = 150\,000$ ) was added in 18 mL of  $N,N$ -dimethyl formamide (DMF) solvent and stirred until dissolved completely. Then, the dissolved solution was carried out by electrospinning with a voltage of 15 kV and a pushing speed of  $0.1\text{ mm min}^{-1}$  to obtain the PAN fibrous membrane. Finally, the CNF membrane was prepared by preoxidation of the PAN fibrous membrane at  $250\text{ }^\circ\text{C}$  for 2 h in an Ar atmosphere and carbonization at  $800\text{ }^\circ\text{C}$  for 2 h. Moreover, by controlling the electrospinning time, CNF membranes with different thicknesses of 40, 100, and  $300\text{ }\mu\text{m}$  were obtained, which were denoted 40-CNF, 100-CNF, and 300-CNF, respectively.

The asymmetric CNF@Ag hosts were prepared by sputtering Ag nanoparticles only on one side of the CNF membrane using an ion sputtering apparatus (JS-1600M, Beijing HTC Technology Co., Ltd.) at a current of 60 mA for various time of 60, 120, and 180 s, which were denoted CNF@Ag-60s, CNF@Ag-120s, and CNF@Ag-180s, respectively.

**2.2. Characterization.** Scanning electron microscope (SEM, Hitachi S-4800) and energy-dispersive X-ray spectroscopy (EDS) were used to observe the morphology and elemental distribution of the samples, respectively. The size of Ag nanoparticles on the surface of CNF was characterized by transmission electron microscopy (TEM, JEM-2100F). The crystal structure and the chemical component of the samples were determined by X-ray diffraction (XRD, Rigaku D/MAX-2550VB), Raman spectroscopy (Renishaw inVia-Reflex, 532 nm radiation), X-ray photoelectron spectroscopy (XPS, Thermo Scientific Escalab 250Xi), and thermogravimetric analysis (TGA, NETZSCH TG 209F1 Libra). For ex situ measurements, the cycled electrodes were first disassembled in a glovebox and repeatedly washed away the remaining electrolyte using pure diglyme or dimethyl carbonate solvent.

**2.3. Theoretical Calculations.** The DFT calculations were performed by the Vienna Ab initio Simulation Package using the projector augmented wave method and the Perdew–Burke–Ernzerhof generalized gradient approximation functional.<sup>30–34</sup> The cutoff energy for the plane wave was set as 450 eV,<sup>25</sup> and the Monkhorst–Pack  $k$ -point sampling grid was  $3 \times 3 \times 1$ . The Ag (five-layer  $3 \times 3 \times 1$  supercell, (111) crystal plane) and  $5 \times 5$  monolayer graphene slabs were constructed as fundamental models for Ag and CNF substrates, respectively.<sup>35,36</sup> Only one Na atom was placed on top of each model and the vacuum layer was 20 Å. The convergence threshold for geometry optimization was set as  $0.01\text{ eV } \text{Å}^{-1}$  in force. The binding energy ( $E_b$ ) between the Na atom and different substrates was calculated using the following equation

$$E_b = E_{\text{Na+slab}} - E_{\text{slab}} - E_{\text{Na}}$$

where  $E_{\text{Na+slab}}$  represents the total energy of a Na atom absorbed with Ag or a graphene slab,  $E_{\text{slab}}$  represents the energy of Ag (111) or a graphene slab, and  $E_{\text{Na}}$  is the energy of a single Na atom. The more negative  $E_b$  value indicates the more stable combination or higher Na affinity.

**2.4. Electrochemical Measurements.** All of the electrochemical tests were carried out using assembled CR2025-type coin cells. Glass fiber (GF/D, Whatman) was chosen as a separator. Unless otherwise noted, 1 M NaPF<sub>6</sub> in diglyme solution (DoDo Chem) with a fixed amount of  $80\text{ }\mu\text{L}$  was applied to each cell.

For evaluating the Na deposition behavior and Coulombic efficiency (CE) of the Cu foil, CNF, or CNF@Ag composite, the half-cells were assembled using a Na disk as a counter electrode. To be noticed, CNF@Ag electrodes were placed in cells with the Ag

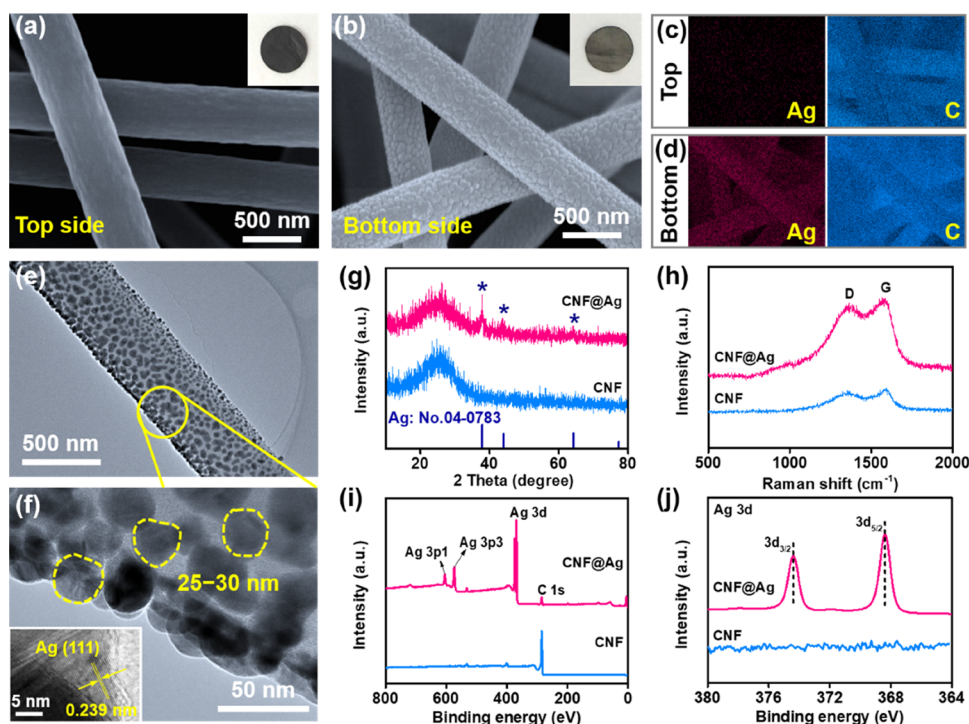


**Figure 2.** SEM images of the CNF@Ag host at (a) top and (b) bottom sides, and (c, d) the corresponding EDS mapping images. (e, f) TEM images of CNF@Ag. The inset of (f) shows the high-resolution TEM image of Ag nanoparticles. (g) XRD patterns and (h) Raman spectra of CNF and CNF@Ag hosts. XPS spectra of CNF and CNF@Ag hosts: (i) full survey and (j) Ag 3d.

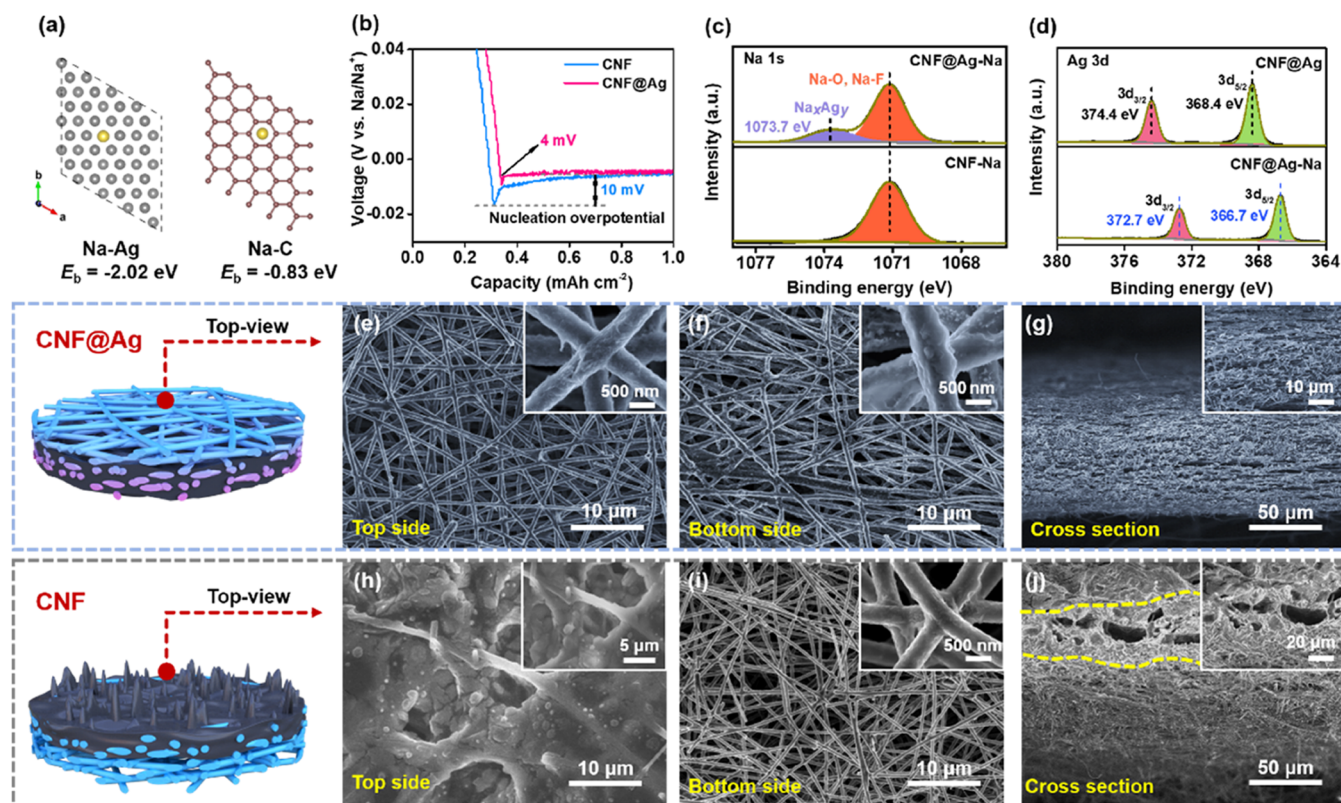


**Figure 3.** Na deposition behavior. (a) Calculated binding energy of the Na atom with the Ag or C atom. (b) The voltage–capacity curves of Na nucleation at 0.5 mA cm<sup>-2</sup> on CNF and CNF@Ag hosts. (c) Na 1s and (d) Ag 3d XPS spectra after Na deposition on CNF and CNF@Ag hosts. Schematic illustrations and SEM images of Na deposition on (e–g) CNF@Ag and (h–j) CNF hosts with a capacity of 4 mAh cm<sup>-2</sup> at 0.5 mA cm<sup>-2</sup>.

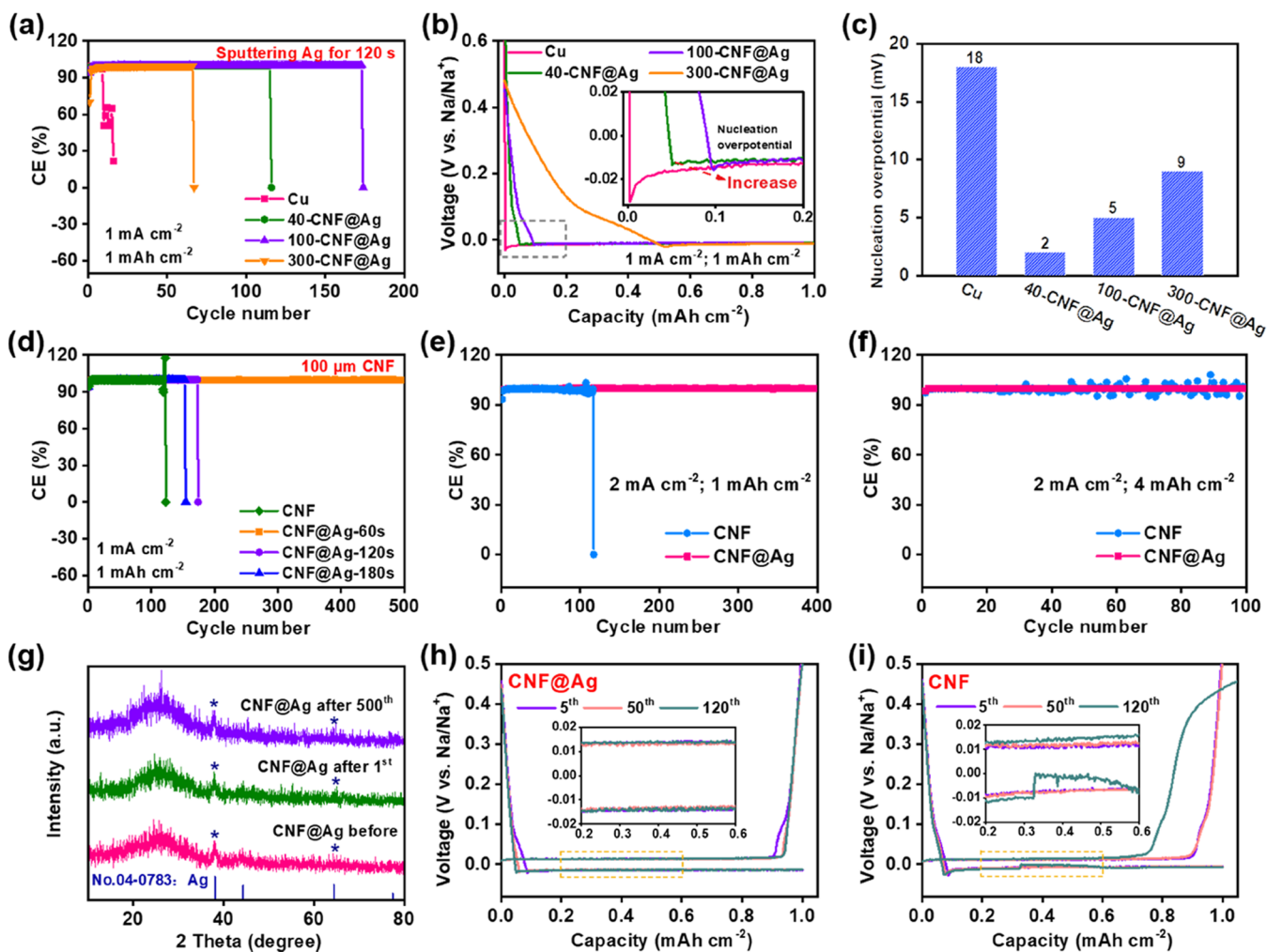


**Figure 4.** Comparisons of (a) CE values, (b) the voltage–capacity curves of Na plating, and (c) nucleation overpotentials of Na deposition on CNF@Ag hosts with different CNF thicknesses and Cu foil. (d) Comparison of CE values for CNF@Ag hosts with different Ag sputtering time. CE tests of CNF and the optimal CNF@Ag hosts at 2 mA cm<sup>-2</sup> for (e) 1 mA cm<sup>-2</sup> and (f) 4 mA cm<sup>-2</sup>. (g) XRD patterns of the CNF@Ag host, and the voltage profiles of (h) CNF@Ag and (i) CNF hosts at different cycles at 1 mA cm<sup>-2</sup> for 1 mA h cm<sup>-2</sup>.

surface away from the separator. To obtain the CE values, the cells were first charged/discharged at 0.01–1.0 V for 3 cycles at 1 mA cm<sup>-2</sup> to stabilize SEI and remove surface contaminations of the electrode. After pretreatment, Na metal was plated on the working electrode with a capacity of 1 mA h cm<sup>-2</sup> at 1 mA cm<sup>-2</sup> and then stripped away by charging the cell to 0.5 V in each galvanostatic cycle.

The CNF-Na and CNF@Ag-Na anodes were obtained by plating Na metal of 4 mA h cm<sup>-2</sup> into the CNF and CNF@Ag hosts at 0.5 mA cm<sup>-2</sup>. Two identical preplated Na metal electrodes were assembled for symmetrical cell tests. Galvanostatic plating/stripping tests were carried out on the LAND battery test system. Electrochemical impedance spectroscopy (EIS) measurements were tested on a CHI600E electrochemical workstation, and the measuring frequency was controlled from 100 kHz to 10 mHz.

For full cell tests, Na<sub>3</sub>V<sub>2</sub>(PO<sub>4</sub>)<sub>3</sub> (NVP) was selected as the cathode to assemble Na//NVP cells. The NVP electrode was synthesized and prepared by a traditional slurry coating method.<sup>37</sup> Typically, the mixture slurry was composed of NVP powder, polyvinylidene fluoride, and Super P (weight ratio of 8:1:1) in *N*-methyl-2-pyrrolidone. These full cells were tested by galvanostatic cycles in a voltage window of 2.0–4.2 V.

### 3. RESULTS AND DISCUSSION

As shown in Figure S1a–c, the electrospun CNF membrane shows a 3D porous structure with a fiber diameter of around

400–500 nm, which can provide a large surface area and an interconnected electron pathway for favorable electrodeposition of Na metal.<sup>38</sup> The thickness of the CNF membrane is tuned by the electrospinning time, ranging from 40 to 300 μm (Figure S1d–f). The asymmetric CNF@Ag host is further obtained through the controllable sputtering of Ag nanoparticles on one side of the CNF membrane. SEM images of the top surface of the CNF@Ag host demonstrate that almost no Ag particles can be found on the very bare surface of CNFs with an extremely weak Ag signal (Figure 2a,c), while Ag nanoparticles are evenly distributed on the surface of carbon fibers at the bottom side of CNF@Ag (Figure 2b,d). In Figure S2, the cross-sectional SEM image and the corresponding EDS mappings of CNF@Ag further confirm that Ag nanoparticles are asymmetrically located at the bottom region of CNF with a thickness of about 30 μm. The TEM images (Figure 2e,f) show that Ag nanoparticles on the surface of CNF@Ag are only 20–30 nm in diameter, which are beneficial to induce the uniform deposition of Na. The high-resolution TEM image further confirms that the lattice fringe with a spacing of 0.239 nm is in good agreement with the (111) plane of metallic Ag (inset of Figure 2f). Figure 2g presents the XRD patterns of CNF and CNF@Ag hosts. The CNF host presents a wide diffraction

peak at about  $2\theta = 26^\circ$ , corresponding to the typical graphitic carbon structure.<sup>39</sup> Meanwhile, the weak peaks at around  $2\theta = 38, 44,$  and  $64^\circ$  in the XRD pattern of CNF@Ag are indexed to Ag (JCPDS 04-0783).<sup>40</sup> The intensity of the characteristic peak of CNF increases in the Raman spectra after Ag sputtering (Figure 2h), which can be ascribed to the surface-enhanced Raman scattering behavior of Ag.<sup>41</sup> XPS spectra analysis also prove the presence of metallic Ag on the surface of CNF@Ag (Figure 2i,j). Both the full survey and Ag 3d spectra of CNF@Ag exhibit distinct Ag peaks. Thus, an asymmetric CNF@Ag host is successfully achieved, where the rationally distributed Ag nanoparticles on the bottom surface of the CNF membrane are critical to selectively regulate the initial nucleation of Na.

To investigate the Na affinity with CNF@Ag and CNF hosts, the binding energies ( $E_b$ ) between the Na atom and Ag or C (representing graphene slab) are calculated by DFT. The binding energy ( $-2.02$  eV) of the Na atom on the Ag (111) surface is lower than that ( $-0.83$  eV) on the pristine CNF surface (Figure 3a), which indicates that the sputtered Ag layer is more sodiophilic than pristine CNF. Hence, CNF@Ag presents a much lower nucleation overpotential of 4 mV than that (10 mV) of the pristine CNF at  $0.5 \text{ mA cm}^{-2}$  as indicated by the dips of the curves in Figure 3b. In addition, the high-resolution Na 1s XPS spectra of CNF and CNF@Ag after Na deposition are shown in Figure 3c. For CNF@Ag-Na, a new signal at 1073.7 eV can be observed, implying that Ag can form alloy phases of  $\text{Na}_x\text{Ag}_y$  by the reaction with Na. Meanwhile, an obvious shift to lower binding energy can be observed in the Ag 3d spectra after Na deposition in CNF@Ag (Figure 3d), further proving the formation of  $\text{Na}_x\text{Ag}_y$  alloy phases. With the identical crystal structure of pure Na metal, the  $\text{Na}_x\text{Ag}_y$  alloy layer can effectively reduce the nucleation barrier for selective nucleation of metallic Na and subsequent growth from bottom to up in the whole electrode.

Na with capacities of 2 and  $4 \text{ mAh cm}^{-2}$  is separately deposited on CNF@Ag and CNF hosts at  $0.5 \text{ mA cm}^{-2}$  to further investigate the Na deposition behavior. For asymmetric CNF@Ag, metallic Na particles are preferentially deposited at the bottom surface with Ag-decorated sites when the deposition capacity is  $2 \text{ mAh cm}^{-2}$  (Figure S3a,b). After increasing the capacity to  $4 \text{ mAh cm}^{-2}$ , subsequent metallic Na is gradually deposited on the existing Na crystals and grows toward the top region of the CNF@Ag host (Figure 3e–g). Notably, the top side of the CNF@Ag composite remains clear with compact Na deposition on the surface of carbon nanofibers, and metallic Na evenly fills up the entire electrode without dendrites. By contrast, a fundamentally different Na deposition behavior can be observed on the CNF electrode. When Na with a capacity of  $2 \text{ mAh cm}^{-2}$  is deposited on the CNF anode, metallic Na tends to accumulate into mossy dendrites distributed on the top surface of the CNF membrane (Figure S3c,d). However, only trace metallic Na is deposited at the bottom of the CNF electrode. With further Na deposition to  $4 \text{ mAh cm}^{-2}$ , a large amount of bulk metallic Na covers the entire top surface of CNF (Figure 3h), but a less amount of metallic Na grows at the bottom region (Figure 3i). The cross-sectional SEM image of the CNF anode further shows that Na directly grows on its top surface with an irregular and loose morphology (Figure 3j), which results from the short pathways for  $\text{Na}^+$  near the separator and unfavorable deposition sites from CNF. For the Cu foil, as a typical anode current collector, the overpotential is 16 mV to overcome the heterogeneous

nucleation barrier (Figure S4). Additionally, the two-dimensional (2D) planar structure has limited deposition sites, inducing Na dendrite deposition on top of the Cu foil (Figure S5). Differing from the Cu foil and CNF, the asymmetric CNF@Ag host can realize relatively flat Na deposition on the separator-away side for safe cells. The distinct Na deposition processes among these three hosts are more directly visualized by an in situ optical cell, as shown in Figure S6. It is noteworthy that Na metal is selectively plated at the bottom region of CNF@Ag without obvious dendrite formation even after a long time of electrodeposition.

As the Na plating/stripping process is closely associated with the thickness and morphology of the sodiophilic layer, CE values of CNF@Ag hosts with different CNF thicknesses and sputtering time of Ag nanoparticles are also tested using a Na disk as the counter electrode. As displayed in Figure 4a, the CE of the control Cu foil electrode appears obviously unstable after only nine cycles and decreases to 21.9% after 16 cycles at  $1 \text{ mA cm}^{-2}$  with a fixed capacity of  $1 \text{ mAh cm}^{-2}$ , on account of its limited surface area with 2D planar construction and a high heterogeneous nucleation barrier. In contrast, all of the CNF@Ag electrodes exhibit high CE values and good stability during cycling. It is noted that the CNF@Ag host with a thickness of  $100 \mu\text{m}$  (denoted 100-CNF@Ag) presents the best stable plating and stripping behaviors for 172 cycles with a high CE value of 99.3%. Properly increasing the thickness of the CNF host can improve its CE. However, the host with a high thickness of  $300 \mu\text{m}$  has a long  $\text{Na}^+$  diffusion pathway and increased nucleation overpotential (Figure 4b,c), thus leading to unfavorable Na plating and stripping. Given the optimized thickness of the CNF host is  $100 \mu\text{m}$ , CNF@Ag hosts prepared by different sputtering time of 60, 120, and 180 s are obtained, which are denoted CNF@Ag-60s, CNF@Ag-120s, and CNF@Ag-180s, respectively. Figure S7 shows that Ag nanoparticles gradually accumulate and become large in size with a long sputtering time. The Ag contents are further determined by Raman spectra (Figure S8a) and TGA (Figure S8b). As shown in Figure 4d, the CE of the pristine CNF electrode shows an obvious fluctuation, ranging from 92.1 to 117.9%, and abruptly decreases to 0% after 118 cycles, indicating the short circuit of the cell, which is caused by the top dendrite piercing separator. By contrast, the cycle lives of CNF@Ag-120s and CNF@Ag-180s are prolonged to 173 and 153 cycles, respectively. In particular, the CNF@Ag-60s electrode still remains stable after 500 cycles with a high CE value of 99.9%. The excellent cycling performance of CNF@Ag-60s can be attributed to the small particle size and a uniform Ag layer as sodiophilic seeds for uniform Na nucleation and growth. Therefore, 100-CNF@Ag-60s is qualified as the optimal host for Na metal anodes, which is abbreviated as CNF@Ag for the following evaluations. By increasing the current density to  $2 \text{ mA cm}^{-2}$  and the capacity to  $4 \text{ mAh cm}^{-2}$ , the CNF@Ag host still exhibits highly stable CE values, much better than the pristine CNF (Figure 4e,f). To reveal the reason for excellent CE, the structure and morphology of CNF@Ag after cycles are further analyzed. In the XRD spectra of CNF@Ag (Figure 4g), the diffraction peak intensity of metallic Ag shows no obvious change before and after the first cycle. Meanwhile, Ag nanoparticles are still uniformly anchored on the surface of CNF (Figure S9a). Even after 500 cycles, the diffraction peaks of Ag can still be detected in CNF@Ag, further indicating that Ag nanoparticles are highly stable on the fibers. With a stable structure of Ag

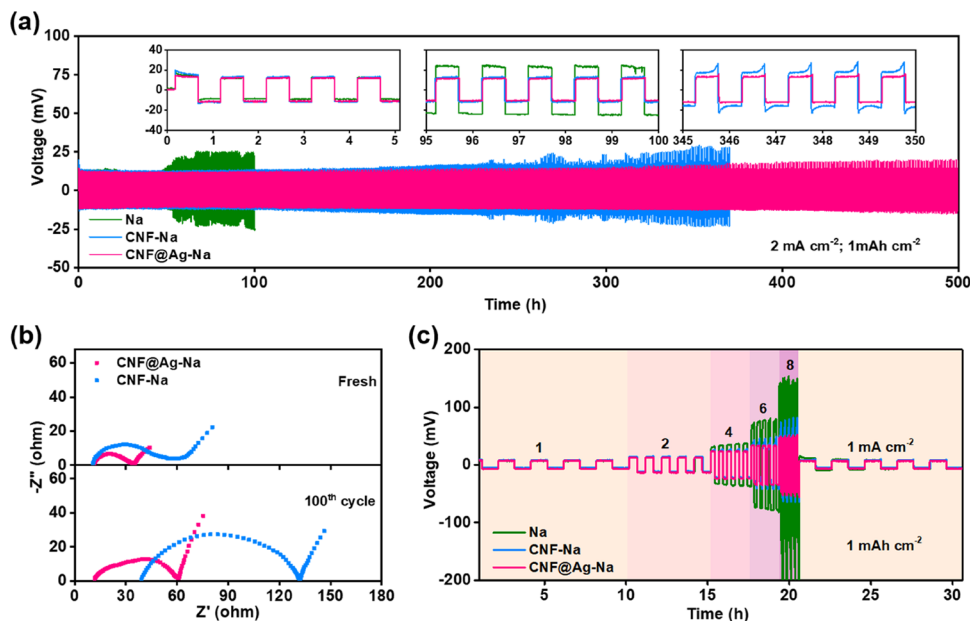


**Figure 5.** Electrochemical performance of symmetric cells. (a) Galvanostatic cycling profiles of the cells at  $2 \text{ mA cm}^{-2}$  for  $1 \text{ mAh cm}^{-2}$ . Insets show the detailed voltage profiles at 0–5, 95–100, and 345–350 h. (b) Nyquist plots of the cells before and after 100 cycles. (c) Rate performance of the cells from 1 to  $8 \text{ mA cm}^{-2}$  with a fixed capacity of  $1 \text{ mAh cm}^{-2}$ .

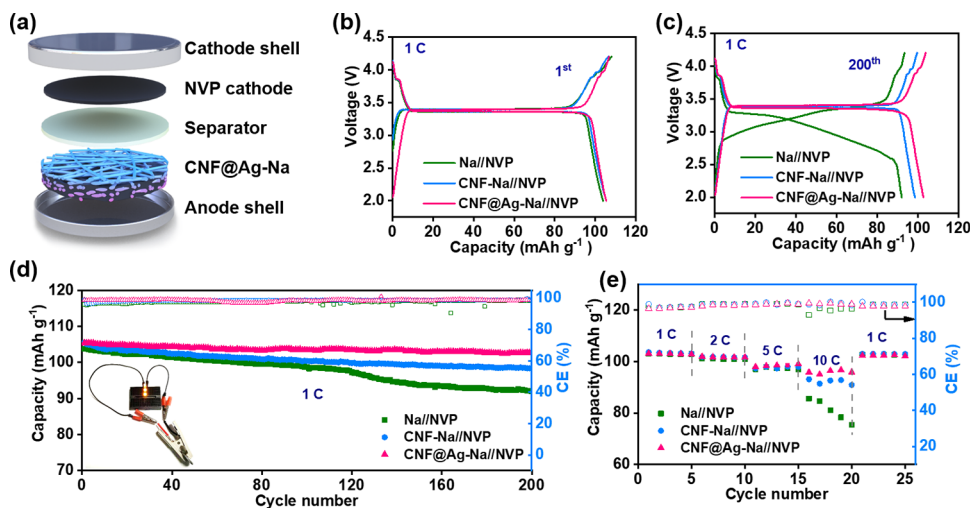


**Figure 6.** Electrochemical performance of the full cell paired with the  $\text{Na}_3\text{V}_2(\text{PO}_4)_3$  cathode. (a) Schematic illustration of full cell assembly. Comparisons of galvanostatic discharge/charge profiles at 1 C for the cells at (b) 1st and (c) 200th cycles. (d) Cycling performance of the cells at 1 C with the inset showing lightened multiple LEDs. (e) Rate performance of the cells from 1 to 10 C.

modification, the top growth of dendrites can be effectively suppressed, thus ensuring the long-term reversible Na plating/stripping in the CNF@Ag host. As demonstrated, the voltage profiles of CNF@Ag remain stable during the cycling process (Figure 4h) and there are no obvious dendrites on the top surface of the electrode (Figure S9b). On the contrary, the voltage profiles of CNF exhibit an obvious fluctuation and the CE is greater than 100% after 120 cycles (Figure 4i). This is possibly because dendritic Na continuously grows and some isolated Na recovers active during the cycling process.<sup>42,43</sup> Thus, abundant dead and mossy Na is distributed on the top surface of the CNF host (Figure S9c).

Symmetric cell tests are further carried out to evaluate the electrochemical performance of bare Na, CNF-Na, and CNF@Ag-Na anodes (Figure 5). For symmetric cells, CNF-Na and CNF@Ag-Na are obtained by the electrochemical deposition

of metallic Na and then reassembled using two same electrodes. Figure 5a shows the cycling performance of symmetric cells at a current density of  $2 \text{ mA cm}^{-2}$  with a capacity of  $1 \text{ mAh cm}^{-2}$ . In the initial few cycles, the three symmetric cells exhibit similar plating/stripping voltage profiles. During the next cycling process, the CNF@Ag-Na symmetric cell can maintain relatively stable Na plating/stripping for 500 h with a small hysteresis of less than 33.8 mV. However, the voltage hysteresis of the bare Na cell rapidly increases to  $\sim 48.5 \text{ mV}$  only after cycling for 100 h. For the CNF-Na symmetric cell, the voltage hysteresis also exhibits a slow increase from  $\sim 26.6$  to  $\sim 50.8 \text{ mV}$  over 350 h owing to the continuous formation of Na dendrites, which leads to an excessive passivation layer on Na/electrolyte and an increase in resistance.<sup>24</sup> To probe the interfacial impedances of CNF-Na and CNF@Ag-Na electrodes, EIS of the symmetric cells before

and after 100 cycles (100 h) is tested. As shown in Figures 5b and S10, the interfacial resistance of the CNF@Ag-Na electrode is smaller and increases slower than that of CNF-Na during cycling. This demonstrates rapid charge transfer in the CNF@Ag-Na electrode with a stable Na/electrolyte interface. When cycling under increasing current densities from 1 to 8 mA cm<sup>-2</sup>, the voltage hysteresis of the CNF@Ag-Na electrode only increases slightly from 14.6 to 102.6 mV (Figure 5c). By contrast, at a high current density of 8 mA cm<sup>-2</sup>, both bare Na and CNF-Na electrodes exhibit relatively large voltage hysteresis values of 383.8 and 143.8 mV, respectively, implying the excellent rate capability of the CNF@Ag-Na electrode. In comparison, the CNF@Ag host exhibits considerable electrochemical performance than those of the reported literature (Tables S1 and S2). In addition, the SEI layers on CNF@Ag-Na and bare Na metal anodes after cycling are further analyzed by comparing the ex situ XPS analysis, as shown in Figure S11. The SEI layer formed on the surface of the two electrodes is the mixture of organic and inorganic components, including RCH<sub>2</sub>ONa, Na<sub>2</sub>O, and NaF. Notably, the SEI layer of the CNF@Ag-Na anode exhibits a higher NaF content (5.42 atom %) than that of the bare Na anode (3.54 atom %), which is more favorable for stable Na plating and stripping.<sup>44,45</sup>

To explore the feasibility of the CNF@Ag-Na anode in practical battery systems, a full cell is assembled by pairing with the Na<sub>3</sub>V<sub>2</sub>(PO<sub>4</sub>)<sub>3</sub> (NVP) cathode (Figure 6a). The full cells with bare Na and CNF-Na anodes are also used as control cells. As shown in Figure 6b–d, the CNF@Ag-Na//NVP full cell achieves an initial discharge capacity of 105.4 mAh g<sup>-1</sup> and can still deliver a high capacity of 102.7 mAh g<sup>-1</sup> with a CE of 99% after 200 cycles at 1 C. However, the discharge capacities of Na//NVP and CNF-Na//NVP decrease to 92 and 98 mAh g<sup>-1</sup> after 200 cycles, respectively. Figure 6e shows the rate performance of the full cells at various current densities from 1 C to 10 C (1 C = 100 mA g<sup>-1</sup>). CNF@Ag-Na//NVP also displays the best rate performance. Especially, when the current density increases to 10 C, the CNF@Ag-Na//NVP full cell still delivers an excellent discharge capacity of 96 mAh g<sup>-1</sup>. Moreover, multiple light-emitting diodes (LEDs) can be lightened by the as-fabricated CNF@Ag-Na//NVP full cell (inset of Figure 6d). These results indicate that the CNF@Ag-Na anode has a promising application in Na metal full batteries.

In addition, the application of the CNF@Ag host for Na metal anodes is further investigated in a carbonate-based electrolyte system. Encouragingly, the asymmetric sodiophilic CNF@Ag host is also effective for inducing preferential Na deposition in the advantageous bottom region (Figure S12), in which there is a lower nucleation overpotential on the sodiophilic Ag particles than that in the pristine CNF host (Figure S13a). Consequently, the CNF@Ag electrode achieves a high Coulombic efficiency of 91.3% after 160 cycles at 1 mA cm<sup>-2</sup> for 1 mAh cm<sup>-2</sup>, showing a stable Na plating and stripping process (Figure S13b–d). In contrast, the cell with the CNF electrode is a failure only after 64 cycles. These results further demonstrate that the asymmetric sodiophilic CNF@Ag host is also advantageous for the Na metal anode in carbonate-based electrolytes.

#### 4. CONCLUSIONS

In summary, we demonstrate that an asymmetric CNF@Ag composite with both sodiophobic and sodiophilic features is a

favorable host for achieving a stable Na metal anode. By facilely sputtering uniform Ag nanoparticles only on the separator-away surface of the CNF matrix, sodiophilic Ag nanoparticles can regulate the preferential nucleation of Na at the bottom surface of the host and realize the uniform and compact Na deposition in the whole anode area with a “bottom-top” mode. As a result, the optimized CNF@Ag host shows high reversibility with an average CE of 99.9% after 500 cycles at a current density of 1 mA cm<sup>-2</sup> for 1 mAh cm<sup>-2</sup>. In addition, the CNF@Ag-Na electrode exhibits excellent electrochemical stability with low and stable interfacial impedance in symmetric cells. Finally, the CNF@Ag-Na//NVP full cell shows good rate and cycling performance, which can effectively improve the safety and stability of the Na metal anode upon long cycling. Moreover, the “bottom-up growth” strategy with the asymmetric sodiophilic CNF@Ag host can also be applied to regulate Na deposition in carbonate-based electrolyte systems.

#### ■ ASSOCIATED CONTENT

##### SI Supporting Information

The Supporting Information is available free of charge at <https://pubs.acs.org/doi/10.1021/acsami.1c13018>.

SEM images of the as-prepared CNF@Ag and CNF hosts; cross-sectional SEM image of the CNF@Ag host and the corresponding EDS mappings; SEM and in situ optical images of Na deposition on CNF@Ag, CNF, and Cu foil; electrochemical data of the CNF@Ag host and Cu foil; and comparison of electrochemical performances between this work and the reported literature (PDF)

#### ■ AUTHOR INFORMATION

##### Corresponding Authors

Yue-E Miao – State Key Laboratory for Modification of Chemical Fibers and Polymer Materials, College of Materials Science and Engineering, Donghua University, Shanghai 201620, China; [orcid.org/0000-0002-3660-029X](https://orcid.org/0000-0002-3660-029X); Email: [yuee\\_miao@dhu.edu.cn](mailto:yuee_miao@dhu.edu.cn)

Tianxi Liu – State Key Laboratory for Modification of Chemical Fibers and Polymer Materials, College of Materials Science and Engineering, Donghua University, Shanghai 201620, China; Key Laboratory of Synthetic and Biological Colloids, Ministry of Education, School of Chemical and Material Engineering, Jiangnan University, Wuxi 214122, China; [orcid.org/0000-0002-5592-7386](https://orcid.org/0000-0002-5592-7386); Email: [txliu@dhu.edu.cn](mailto:txliu@dhu.edu.cn)

##### Authors

Lulu Mo – State Key Laboratory for Modification of Chemical Fibers and Polymer Materials, College of Materials Science and Engineering, Donghua University, Shanghai 201620, China

Ai-Long Chen – State Key Laboratory for Modification of Chemical Fibers and Polymer Materials, College of Materials Science and Engineering, Donghua University, Shanghai 201620, China

Yue Ouyang – State Key Laboratory for Modification of Chemical Fibers and Polymer Materials, College of Materials Science and Engineering, Donghua University, Shanghai 201620, China

Wei Zong – State Key Laboratory for Modification of Chemical Fibers and Polymer Materials, College of Materials Science and Engineering, Donghua University, Shanghai 201620, China

Complete contact information is available at:  
<https://pubs.acs.org/10.1021/acsami.1c13018>

### Author Contributions

L.M. and Y.-E.M. conceived the idea. L.M. performed the experiments, contributed to data analysis, and wrote the manuscript. A.-L.C. performed the partial experiments and tests. Y.O. and W.Z. contributed to data analysis. Y.-E.M. contributed to theoretical analysis, supervision, and editing. T.L. contributed to supervision and editing. All authors contributed to general discussions.

### Notes

The authors declare no competing financial interest.

### ACKNOWLEDGMENTS

The authors are grateful for the financial support from the National Natural Science Foundation of China (22075042), the Natural Science Foundation of Shanghai (20ZR1401400), and the Fundamental Research Funds for the Central Universities and DHU Distinguished Young Professor Program (LZB2021002).

### REFERENCES

- (1) Tarascon, J. M.; Armand, M. Issues and Challenges Facing Rechargeable Lithium Batteries. *Nature* **2001**, *414*, 359–367.
- (2) Bruce, P. G.; Scrosati, B.; Tarascon, J. M. Nanomaterials for Rechargeable Lithium Batteries. *Angew. Chem., Int. Ed.* **2008**, *47*, 2930–2946.
- (3) Slater, M. D.; Kim, D.; Lee, E.; Johnson, C. S. Sodium-Ion Batteries. *Adv. Funct. Mater.* **2013**, *23*, 947–958.
- (4) Kim, S. W.; Seo, D. H.; Ma, X.; Ceder, G.; Kang, K. Electrode Materials for Rechargeable Sodium-Ion Batteries: Potential Alternatives to Current Lithium-Ion Batteries. *Adv. Energy Mater.* **2012**, *2*, 710–721.
- (5) Liu, T.; Zhang, Y.; Jiang, Z.; Zeng, X.; Ji, J.; Li, Z.; Gao, X.; Sun, M.; Lin, Z.; Ling, M.; Zheng, J.; Liang, C. Exploring Competitive Features of Stationary Sodium Ion Batteries for Electrochemical Energy Storage. *Energy Environ. Sci.* **2019**, *12*, 1512–1533.
- (6) Luo, W.; Hu, L. Na Metal Anode: "Holy Grail" for Room-Temperature Na-Ion Batteries? *ACS Cent. Sci.* **2015**, *1*, 420–422.
- (7) Zheng, X.; Bommier, C.; Luo, W.; Jiang, L.; Hao, Y.; Huang, Y. Sodium Metal Anodes for Room-Temperature Sodium-Ion Batteries: Applications, Challenges and Solutions. *Energy Storage Mater.* **2019**, *16*, 6–23.
- (8) Zhao, Y.; Adair, K. R.; Sun, X. L. Recent Developments and Insights into the Understanding of Na Metal Anodes for Na-Metal Batteries. *Energy Environ. Sci.* **2018**, *11*, 2673–2695.
- (9) Zhao, C.; Lu, Y. L.; Yue, J. Y.; Pan, D. P.; Qi, Y. Q.; Hu, Y. S.; Chen, L. C. Advanced Na Metal Anodes. *J. Energy Chem.* **2018**, *27*, 1584–1596.
- (10) Fan, L.; Li, X. Recent Advances in Effective Protection of Sodium Metal Anode. *Nano Energy* **2018**, *53*, 630–642.
- (11) Boschini, A.; Abdelhamid, M. E.; Johansson, P. On the Feasibility of Sodium Metal as Pseudo-Reference Electrode in Solid State Electrochemical Cells. *ChemElectroChem* **2017**, *4*, 2717–2721.
- (12) Wang, H.; Matios, E.; Luo, J.; Li, W. Combining Theories and Experiments to Understand the Sodium Nucleation Behavior Towards Safe Sodium Metal Batteries. *Chem. Soc. Rev.* **2020**, *49*, 3783–3805.
- (13) Wei, S.; Choudhury, S.; Xu, J.; Nath, P.; Tu, Z.; Archer, L. A. Highly Stable Sodium Batteries Enabled by Functional Ionic Polymer Membranes. *Adv. Mater.* **2017**, *29*, No. 1605512.

(14) Ferdousi, S. A.; O'Dell, L. A.; Hilder, M.; Barlow, A. J.; Armand, M.; Forsyth, M.; Howlett, P. C. SEI Formation on Sodium Metal Electrodes in Superconcentrated Ionic Liquid Electrolytes and the Effect of Additive Water. *ACS Appl. Mater. Interfaces* **2021**, *13*, 5706–5720.

(15) Zhao, Y.; Goncharova, L. V.; Lushington, A.; Sun, Q.; Yadegari, H.; Wang, B.; Xiao, W.; Li, R.; Sun, X. Superior Stable and Long Life Sodium Metal Anodes Achieved by Atomic Layer Deposition. *Adv. Mater.* **2017**, *29*, No. 1606663.

(16) Choudhury, S.; Wei, S.; Ozhaves, Y.; Gunceler, D.; Zachman, M. J.; Tu, Z.; Shin, J. H.; Nath, P.; Agrawal, A.; Kourkoutis, L. F.; Arias, T. A.; Archer, L. A. Designing Solid-Liquid Interphases for Sodium Batteries. *Nat. Commun.* **2017**, *8*, No. 898.

(17) Ling, W.; Fu, N.; Yue, J.; Zeng, X. X.; Ma, Q.; Deng, Q.; Xiao, Y.; Wan, L. J.; Guo, Y. G.; Wu, X. W. A Flexible Solid Electrolyte with Multilayer Structure for Sodium Metal Batteries. *Adv. Energy Mater.* **2020**, *10*, No. 1903966.

(18) Ye, H.; Wang, C. Y.; Zuo, T. T.; Wang, P. F.; Yin, Y. X.; Zheng, Z. J.; Wang, P.; Cheng, J.; Cao, F. F.; Guo, Y. G. Realizing a Highly Stable Sodium Battery with Dendrite-Free Sodium Metal Composite Anodes and O<sub>3</sub>-Type Cathodes. *Nano Energy* **2018**, *48*, 369–376.

(19) Zheng, X.; Li, P.; Cao, Z.; Luo, W.; Sun, F.; Wang, Z.; Ding, B.; Wang, G.; Huang, Y. Boosting the Reversibility of Sodium Metal Anode via Heteroatom-Doped Hollow Carbon Fibers. *Small* **2019**, *15*, No. 1902688.

(20) Wu, F.; Zhou, J.; Luo, R.; Huang, Y.; Mei, Y.; Xie, M.; Chen, R. Reduced Graphene Oxide Aerogel as Stable Host for Dendrite-Free Sodium Metal Anode. *Energy Storage Mater.* **2019**, *22*, 376–383.

(21) Wu, W.; Hou, S.; Zhang, C.; Zhang, L. A Dendrite-free Na-Na<sub>2</sub>S-Carbon Hybrid toward a Highly Stable and Superior Sodium Metal Anode. *ACS Appl. Mater. Interfaces* **2020**, *12*, 27300–27306.

(22) Ma, C.; Xu, T.; Wang, Y. Advanced Carbon Nanostructures for Future High Performance Sodium Metal Anodes. *Energy Storage Mater.* **2020**, *25*, 811–826.

(23) Zou, P.; Chiang, S. W.; Zhan, H.; Sui, Y.; Liu, K.; Hu, S.; Su, S.; Li, J.; Kang, F.; Yang, C. A Periodic "Self-Correction" Scheme for Synchronizing Lithium Plating/Stripping at Ultrahigh Cycling Capacity. *Adv. Funct. Mater.* **2020**, *30*, No. 1910532.

(24) Pu, J.; Li, J.; Zhang, K.; Zhang, T.; Li, C.; Ma, H.; Zhu, J.; Braun, P. V.; Lu, J.; Zhang, H. Conductivity and Lithiophilicity Gradients Guide Lithium Deposition to Mitigate Short Circuits. *Nat. Commun.* **2019**, *10*, No. 1896.

(25) Wu, J.; Zou, P.; Ihsan-Ul-Haq, M.; Mubarak, N.; Susca, A.; Li, B.; Ciucci, F.; Kim, J. K. Sodiophilically Graded Gold Coating on Carbon Skeletons for Highly Stable Sodium Metal Anodes. *Small* **2020**, *16*, No. 2003815.

(26) Sun, Z.; Jin, H.; Ye, Y.; Xie, H.; Jia, W.; Jin, S.; Ji, H. Guiding Sodium Deposition through a Sodiophobic-Sodiophilic Gradient Interfacial Layer for Highly Stable Sodium Metal Anodes. *ACS Appl. Energy Mater.* **2021**, *4*, 2724–2731.

(27) Hu, G.; Zhang, X.; Liu, X.; Yu, J.; Ding, B. Strategies in Precursors and Post Treatments to Strengthen Carbon Nanofibers. *Adv. Fiber Mater.* **2020**, *2*, 46–63.

(28) Zong, W.; Lian, R.; He, G.; Guo, H.; Ouyang, Y.; Wang, J.; Lai, F.; Miao, Y.; Rao, D.; Brett, D.; Liu, T. Vacancy Engineering of Group VI Anions in NiCo<sub>2</sub>A<sub>4</sub> (A = O, S, Se) for Efficient Hydrogen Production by Weakening the Shackles of Hydronium Ion. *Electrochim. Acta* **2020**, *333*, No. 135515.

(29) Liu, L.; Xu, W.; Ding, Y.; Agarwal, S.; Greiner, A.; Duan, G. A Review of Smart Electrospun Fibers toward Textiles. *Compos. Commun.* **2020**, *22*, No. 100506.

(30) Kresse, G.; Hafner, J. *Ab Initio* Molecular-Dynamics Simulation of the Liquid-Metal-Amorphous-Semiconductor Transition in Germanium. *Phys. Rev. B* **1994**, *49*, 14251–14269.

(31) Kresse, G.; Furthmüller, J. Efficient Iterative Schemes for *Ab Initio* Total-Energy Calculations Using a Plane-Wave Basis Set. *Phys. Rev. B* **1996**, *54*, 11169–11186.

(32) Blöchl, P. E. Projector Augmented-Wave Method. *Phys. Rev. B* **1994**, *50*, 17953–17979.

(33) Kresse, G.; Joubert, D. From Ultrasoft Pseudopotentials to the Projector Augmented-Wave Method. *Phys. Rev. B* **1999**, *59*, 1758–1775.

(34) Hammer, B.; Hansen, L. B.; Norskov, J. K. Improved Adsorption Energetics within Density-Functional Theory Using Revised Perdew-Burke-Ernzerhof Functionals. *Phys. Rev. B* **1999**, *59*, 7413–7421.

(35) Wang, H.; Wu, Y.; Liu, S.; Jiang, Y.; Shen, D.; Kang, T.; Tong, Z.; Wu, D.; Li, X.; Lee, C. S. 3D Ag@C Cloth for Stable Anode Free Sodium Metal Batteries. *Small Methods* **2021**, *5*, No. 2001050.

(36) Zhang, R.; Chen, X.; Shen, X.; Zhang, X.; Chen, X.; Cheng, X.; Yan, C.; Zhao, C.; Zhang, Q. Coralloid Carbon Fiber-Based Composite Lithium Anode for Robust Lithium Metal Batteries. *Joule* **2018**, *2*, 764–777.

(37) Zhu, L.; Sun, Q.; Xie, L.; Cao, X.  $\text{Na}_3\text{V}_2(\text{PO}_4)_3$ @NC Composite Derived from Polyaniline as Cathode Material for High-Rate and Ultralong-Life Sodium-Ion Batteries. *Int. J. Energy Res.* **2020**, *44*, 4586–4594.

(38) Lai, F.; Huang, Y.; Miao, Y.; Liu, T. Controllable Preparation of Multi-Dimensional Hybrid Materials of Nickel-Cobalt Layered Double Hydroxide Nanorods/Nanosheets on Electrospun Carbon Nanofibers for High-Performance Supercapacitors. *Electrochim. Acta* **2015**, *174*, 456–463.

(39) Zhu, T.; Feng, Q.; Liu, S.; Zhang, C. Metallogel-Derived 3D Porous Carbon Nanosheet Composites as an Electrocatalyst for Oxygen Reduction Reaction. *Compos. Commun.* **2020**, *20*, No. 100376.

(40) Wang, X.; Pan, Z.; Wu, Y.; Xu, G.; Zheng, X.; Qiu, Y.; Liu, M.; Zhang, Y.; Li, W. Reducing Lithium Deposition Overpotential with Silver Nanocrystals Anchored on Graphene Aerogel. *Nanoscale* **2018**, *10*, 16562–16567.

(41) Cheng, Y.; Wang, D.; Mei, Y.; Sun, F. Ag–Cu@Fa Hydrogel-Nanocomposites as Catalyst and Sens Substrate for the Oxidation of TMB. *Compos. Commun.* **2020**, *22*, No. 100485.

(42) Zheng, Z.; Zeng, X.; Ye, H.; Cao, F.; Wang, Z. Nitrogen and Oxygen Co-Doped Graphitized Carbon Fibers with Sodiophilic-Rich Sites Guide Uniform Sodium Nucleation for Ultrahigh-Capacity Sodium-Metal Anodes. *ACS Appl. Mater. Interfaces* **2018**, *10*, 30417–30425.

(43) Hong, S. H.; Jung, D. H.; Kim, J. H.; Lee, Y. H.; Cho, S. J.; Joo, S. H.; Lee, H. W.; Lee, K. S.; Lee, S. Y. Electrical Conductivity Gradient Based on Heterofibrous Scaffolds for Stable Lithium-Metal Batteries. *Adv. Funct. Mater.* **2020**, *30*, No. 1908868.

(44) Zhang, X.; Hao, F.; Cao, Y.; Xie, Y.; Yuan, S.; Dong, X.; Xia, Y. Dendrite-Free and Long-Cycling Sodium Metal Batteries Enabled by Sodium-Ether Cointercalated Graphite Anode. *Adv. Funct. Mater.* **2021**, *31*, No. 2009778.

(45) He, X.; Jin, S.; Miao, L.; Cai, Y.; Hou, Y.; Li, H.; Zhang, K.; Yan, Z.; Chen, J. A 3D Hydroxylated MXene/Carbon Nanotubes Composite as a Scaffold for Dendrite-Free Sodium-Metal Electrodes. *Angew. Chem., Int. Ed.* **2020**, *59*, 16705–16711.